

## A prototype of 2 $\mu\text{m}$ balanced detector for Space-borne Coherent Doppler Wind Lidar

Chen Baolin<sup>1</sup>, Jin Ge<sup>1,3</sup>, Wang Chong<sup>2</sup>, Chen Lian<sup>4</sup>

- (1. School of Physics Sciences, University of Science and Technology of China, Hefei 230026, China;
2. School of Earth and Space Sciences, University of Science and Technology of China, Hefei 230026, China;
3. Hefei National Laboratory, Hefei 230026, China;
4. School of Nuclear Science and Technology, Lanzhou University, Lanzhou 730000, China)

**Abstract:** Despite rapid advancements in lidar technology, extremely long-range observation remains a significant challenge. Recently, 2  $\mu\text{m}$  lasers have demonstrated a potential to be applied in CDWL (Coherent Doppler Wind Lidar) system, for its high atmospheric penetration capability through the atmosphere and high potential laser power. In this study, we present a 2  $\mu\text{m}$  balanced detector that consists of a pair of commercial positive-intrinsic-negative (PIN) diodes with a low-noise transimpedance circuit. To meet the high bandwidth requirements, the highspeed transimpedance circuit and bias voltage tuning method were utilized to overcome the large capacitance of PIN diodes. The circuit transfer function, stability analysis and noise calculation have been studied. The detector was co-packaged with a data acquisition module for convenient data transmission and bias voltage control. The characteristics of the detector, including bandwidth, noise and bias voltage influence, are evaluated in laboratory. Results show that the RMS value of the balanced detector background noise is 539  $\mu\text{V}$  and the bandwidths of the two diodes are 110.8 MHz and 110.3 MHz, respectively. The evaluation results show that the balanced detector meets the wind measurement requirements and allows for a 1.45 $\times$  increase in bandwidth through bias voltage tuning. Our work offers insights into lidar detector design and bandwidth enhancement, providing a valuable reference for researchers and professionals in the field. More importantly, it lays a critical foundation for future ultra-long-range and space-borne 2 $\mu\text{m}$  coherent wind lidar systems by addressing key device-level challenges. PACS codes Each manuscript must be given 2-4 PACS codes below the abstract, the principal index code should be placed first. PACS codes are available on: <http://www.aip.org/pacs/>

**Key words:** Balanced detector, Transimpedance circuit, CDWL, Laser detection

**PACS:**

## 用于 2 $\mu\text{m}$ 波长星载相干多普勒风激光雷达的平衡探测器原型样机

—陈宝林<sup>1</sup>, 金革<sup>1,3</sup>, 王冲<sup>2</sup>, 陈炼<sup>4</sup>

陈宝林, 金革, 王冲, 陈炼

1. 物理学院, 中国科学技术大学, 230026, 中国
2. 地球和空间科学学院, 中国科学技术大学, 230026, 中国
3. 合肥国家实验室, 230026, 中国
4. 核科学与技术学院, 兰州大学, 730000, 中国

**Abstract:** 尽管激光雷达技术迅速发展, 但超长距离观测仍然是一个重大挑战。最近, 2 $\mu\text{m}$  激光器因其穿过大气的高大气穿透能力和高潜在激光功率, 被证明有可能应用于相干多普勒风激光雷达 (CDWL) 系统。在本文中, 我们提出了一种 2 $\mu\text{m}$  平衡探测器, 由一对光电 PIN 二极管和低噪声跨阻抗电路组成。为了满足高带宽要求, 利用高速跨阻抗电路和偏置电压调

谐方法来克服 PIN 二极管的大电容。对电路传递函数、稳定性分析和噪声计算进行了研究。该探测器与数据采集模块共同封装, 便于数据传输和偏置电压控制。然后在实验室评估了探测器的特性, 包括带宽、噪声和偏置电压的影响。结果表明, 平衡探测器背景噪声的均方根值为 539  $\mu\text{V}$ , 两个二极管的带宽分别为 110.8 MHz 和 110.3 MHz。这满足了风测量要求, 并允许通过偏置电压调谐实现更高的带宽, 使得带宽相对于零偏压模式提升 1.45 倍。我们的工作为激光雷达探测器设计和带宽增强提供了见解, 并为该领域的研究人员和专业人士提供了宝贵的参考, 为未来的超远距离和星载 2 $\mu\text{m}$  相干风激光雷达提供了关键器件

支持。

**Key words:** 平衡探测器、跨阻放大器、相干多普勒激光雷达、激光探测

## 1 Introduction

In recent decades, wind lidar has become widely used in various application, such as environment observation, wind measurement, atmosphere research and aviation safety<sup>[1-4]</sup>. To meet the application requirements, wind lidar pursues higher detection range, distance resolution, data accuracy and faster acquisition rates. In the context of detection regimes, wind lidar can be categorized into two types: direct detection and coherent detection<sup>[5]</sup>. The direct detection utilizes spectrometers to resolve the doppler frequency shift mainly from molecular Rayleigh backscatter, which typically operated with visible and ultraviolet laser. The Aeolus lidar, so-called ALADIN, operates in ultraviolet (UV) at 0.355  $\mu\text{m}$ . It is a direct detection lidar and developed by the European Space Agency<sup>[6]</sup>, which intends to provide wind data evenly distributed everywhere in the lower atmosphere (below 30 km altitude). Despite challenges such as systematic errors affecting data quality at the beginning of the mission, Aeolus surpassed its planned lifetime of three years and proved invaluable for weather prediction and scientific research until its conclusion<sup>[7]</sup>.

The coherent detection regime utilizes the interference between aerosol Mie backscatter and local oscillator beam to retrieve the doppler frequency shift, which results in a narrower spectrum peak, enabling higher resolution in wind speed measurements. Different from direct detection, it requires a balanced detector to transform the interference into electric signal, enabling following signal digitization and data processing. Wind lidar using coherent detection is called Coherent Doppler Wind Lidar (CDWL), and many experiments have been conducted based on this technology<sup>[8,9]</sup>. Canadillas performs a offshore wind farm cluster wakes observation with the CDWL, which aims to demonstrate the system performance and thus quantify cluster wake effects reliably<sup>[10]</sup>. Although many comparative experiments have shown that CDWL can generate reliable wind data with respect to the other observation instruments, there remains a challenge for application in extremely long range detection, such as global observation on satellite<sup>[11-13]</sup>. As the distance increases, data accuracy may be compromised and can become unreliable due to low signal-to-noise ratio (SNR)<sup>[14-16]</sup>.

Despite suppressing the system noise, increasing the aerosol backscatter intensity appears to be the primary approach to enhance the SNR, which requires higher laser emittance power and reduced energy loss during laser propagation. In addition, increasing the receive efficiency is also a complementary method to increase the SNR, including increasing the aperture radius and employing high-quantum-efficiency detector. However, increasing the telescope aperture is not always practical, especially in volume-sensitive applications.

Recently, 2  $\mu\text{m}$  wavelength lasers have shown poten-

tial to be applied in future CDWL system, for its high atmospheric penetration capability through the atmosphere. Meanwhile, 2  $\mu\text{m}$  solid-state lasers are expected to achieve an order of magnitude higher output power than conventional 1.5  $\mu\text{m}$  lasers. Additionally, according to the Doppler equation, the bandwidth requirements for a detector operating at a 2  $\mu\text{m}$  wavelength decrease to three-fourths of those for a detector operating at a 1.5  $\mu\text{m}$  wavelength. To fully realize the potential of the 2  $\mu\text{m}$  CDWL, a 2  $\mu\text{m}$  balanced detector is essential for further development, which enables efficient signal detection and system optimization. The previous balanced detector worked at visible and 1.5  $\mu\text{m}$  wavelengths, which are not compatible with the 2  $\mu\text{m}$  CDWL<sup>[17-19]</sup>. Currently, our research focus is on the device-level development and performance optimization in the 2  $\mu\text{m}$  wavelength band, while system-level studies still face some technical challenges, particularly in laser technology. At present, the development of high-performance 2  $\mu\text{m}$  lasers in China is not yet mature, which limits the progress of system integration experiments. Nevertheless, our team has accumulated extensive system-level research experience in other mature wavelength bands, such as 1550 nm and 1064 nm<sup>[20][21][22]</sup>. Therefore, although hardware limitations prevent us from conducting system-level experiments at 2  $\mu\text{m}$ , we can still evaluate the performance of our 2  $\mu\text{m}$  detectors through simulations and empirical assessments.

In this paper, we have designed a 2  $\mu\text{m}$  balanced detector, which integrated a pair of commercial Positive-Intrinsic-Negative (PIN) diodes with a read-out transimpedance circuit and a data acquisition module. It is expected to be utilized to develop a 2  $\mu\text{m}$  CDWL system. To meet the wind measurement requirements, the detector needs to achieve a novel performance with high detection efficiency, high bandwidth and low noise. The paper is organized as follows. The first section is the introduction. In the second section, the CDWL theory and the requirements are presented and analyzed. In the third section, the circuit simulation and the design of the detector are presented. In the fourth section, the test setup has been introduced and a evaluation of the detector has been conducted, followed by results discussion. In the last section, conclusion and outlooks are given.

## 2 Principle and requirements

A typical CDWL system diagram is shown in Fig. 1, which consists of a laser optical module, a balanced detector, a data acquisition module and a host PC. During working, continuous laser generated by seed laser split into beam 1 and beam 2 at the beam splitter. The first beam, referred to as beam 1, was modulated by AOM, generating a pulsed beam output. Sequentially, the pulsed beam was amplified by EDFA and emitted into the atmosphere. Then the pulsed beam was scattered with the aerosols, generating Mie backscatter. The second beam, referred to as beam 2, serves as the local oscillator beam. The backscattered light and the local oscillator beam are directed to the balanced detector after mixing in

a 2×2 beam combiner. In the detector, the interference is detected and transformed into an electrical signal. Next, the electrical signal is digitized by a data acquisition module (DAQ) and transferred to a host PC for post-processing, including FFT (Fast Fourier Transform), power spectral analysis and wind retrieve. Due to the Doppler effect<sup>[23]</sup>, a frequency shift  $\Delta f$  can be extracted as Eq. (1)

$$\Delta f = |f_{\text{interference}} - f_{\text{modulation}}| = \frac{2v}{\lambda} \quad (1)$$

In this equation,  $v$  is the aerosol velocity,  $\lambda$  is the laser wavelength,  $f_{\text{interference}}$  is the interference spectrum peak frequency, and  $f_{\text{modulation}}$  is the AOM modulation frequency.

To achieve precise interference frequency extraction, a balanced detector is required to convert the interference into a voltage-output signal, which is the only form that can be digitized by common data acquisition devices. To avoid information loss, the balanced detector must have a detection capability with compatible bandwidth, ensuring low noise performance. As described by Eq. (1), a 1 m/s variation in wind velocity corresponds to a 1 MHz variation of the  $f_{\text{backscatter}}$  at the 2  $\mu\text{m}$  wavelength, where  $f_{\text{backscatter}}$  denotes the frequency of the backscattered signal. In general, the horizontal wind speed in the atmosphere ranges from -30 to 30 m/s. However, typhoon and tornado sometimes reach speeds of up to 10<sup>2</sup> m/s. In most cases, the doppler frequency range is  $\pm 30$  MHz. Since the modulation frequency is typically set to 80 MHz to achieve high-efficiency modulation, a detector bandwidth of 110 MHz is required. For weak signals in long-range observation, incoherent spectrum accumulation within a range gate is critical to distinguish the signal from noise. In addition, the conversion gain is a critical parameter for the balanced detector. However, there is a tradeoff between the conversion gain and the circuit bandwidth, as detailed in the next section.

### 3 Detector design

#### 3.1 Read-out circuit

Conventionally, there are two methods to implement I-V conversion for current-generating sensors like PIN diodes<sup>[17]</sup>. The first approach is to directly connect a resistor

at the sensor output, which is simple and cost-effective. In this configuration, the -3 dB bandwidth can be calculated as

$$F = \frac{1}{2\pi RC_d} \quad (2)$$

, where  $C_d$  is the capacitance of detector,  $R$  is the resistor value. However, it has some drawbacks. The diode bias voltage varies with the output voltage, which may introduce unwanted nonlinearities in the output and affect the operating condition of the diode. In addition, the input impedance of digitization devices can significantly influence the circuit gain coefficient, potentially reducing the overall performance.

To address these limitations, a transimpedance circuit is a more favorable solution. Compared with the first type of I-V circuit, this approach provides a larger bandwidth and reliable diode bias voltage control. As shown in Fig. 2, the two diodes are modeled as a current source  $I_d$  in parallel with a capacitance  $C_d$ . An operational amplifier configured as a transimpedance amplifier is used to convert the current into a voltage output. The operational amplifier's input parasitic capacitances, including common-mode capacitance and differential-mode capacitance, are considered and denoted by  $C_{cm}$  and  $C_{diff}$ , respectively. For simplicity, the open-loop gain curve  $A(s)$  of the operation amplifier is expressed as

$$A(s) = \frac{A_{OL}\omega_A}{s + \omega_A} \quad (3)$$

, in which  $A_{OL}\omega_A = 2\pi \cdot \text{GBP}$  and  $\omega_A$  represents the open-loop gain cutoff frequency. The gain-bandwidth product (GBP), a key metric for operational amplifiers, equals the product of the open-loop gain and the bandwidth and determines the amplifier's maximum usable frequency. Then the circuit transfer function is derived as Eq. (4). The quality factor  $Q$ ,  $\omega_0$ , and  $C_s$  are defined by Eq. (5), Eq. (6) and Eq. (7), respectively.

$$\frac{V_o}{I_d} = R_f \frac{A_{OL}}{A_{OL} + 1} \frac{\omega_0^2}{s^2 + s \frac{\omega_0}{Q} + \omega_0^2} \quad (4)$$

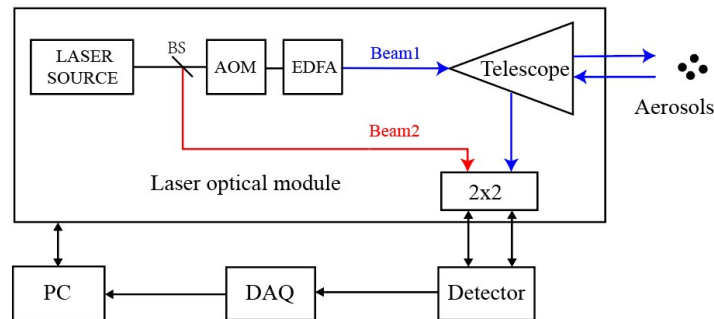


Fig. 1 Typical CDWL system diagram. : BS, beam splitter; AOM, Acousto-Optic Modulator; EDFA, Erbium-Doped Fiber Amplifier; DAQ, data acquisition module;

图1 典型相干激光雷达系统框图

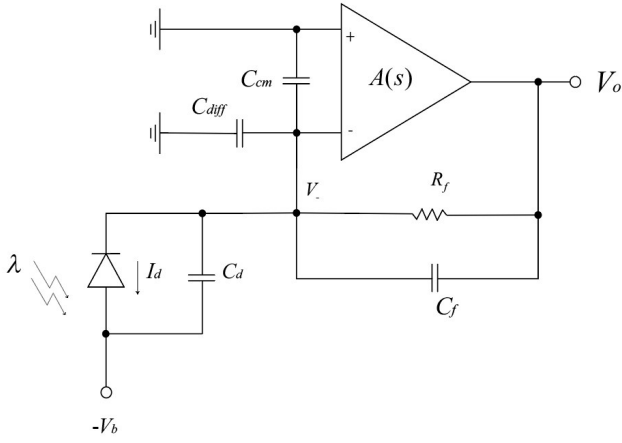


Fig. 2 The transimpedance circuit model.  
图2 跨阻电路模型

$$Q = \frac{\sqrt{\frac{(A_{OL} + 1)\omega_A}{R_f(C_s + C_f)}}}{\omega_A \left(1 + A_{OL} \frac{C_f}{C_s + C_f}\right) + \frac{1}{R_f(C_s + C_f)}} \quad (5)$$

$$\omega_0 = \sqrt{\frac{(A_{OL} + 1)\omega_A}{R_f(C_s + C_f)}} \quad (6)$$

$$C_s = C_{diff} + C_{cm} + C_d \quad (7)$$

The transfer function characterizes the frequency response of the circuit and describes the relationship between the input and output signals. It's worth noting that Eq. (4) represents a second-order Butterworth function. The quality factor  $Q$  can be adjusted by tuning the value of  $C_f$  as described in Eq. (5), thereby modifying the frequency response. Using Matlab, frequency response curves for different  $Q$  values were generated through simulation. As shown in Fig. 3, the x-axis represents the normalized frequency, while the y-axis shows the corresponding frequency response value. When  $Q$  is set to 0.707, corresponding to the maximally flat magnitude response of a Butterworth filter, the frequency response becomes significantly flatter compared to the case when  $Q$  is 1.5, ensuring a precise wind speed extraction.

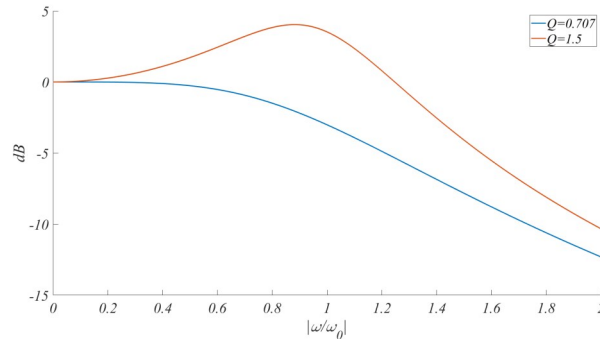


Fig. 3 Frequency response curves with different  $Q$  values.  
图3 不同品质因子下的频率响应曲线

The bandwidth, given by  $\omega_0/2\pi$ , is determined by the values of GBP,  $R_f$ ,  $C_s$ , as implied by Eq. (6). The larger the GBP, the larger the bandwidth. Therefore an operational amplifier with a high GBP is required to meet the wind observation requirements. Next,  $R_f$  could be adjusted under the condition of maintaining circuit stability. Moreover, the detector capacitance  $C_d$ , which is the primary contribution of  $C_s$ , could be adjusted through the bias voltage, which may also introduce a fluctuation of dark noise.

As the bias voltage changes from 0 to -1 V, causing the dark current to vary from 4 nA to 20 nA, the increase in noise in the output due to bias voltage variation is no more than 16  $\mu$ V when  $R_f$  is set to 1 k $\Omega$ . This increase is negligible compared to other sources of noise. Therefore, tuning the bias voltage is a viable option for bandwidth adjustment.

### 3.2 Circuit stability analysis

The high GBP of the operational amplifier, combined with nonlinear transfer characteristics, necessitates extended stability analysis in transimpedance circuits, where phase margin serves as the key metric. As shown in Fig. 4, a co-plot of the open-loop gain curve and noise gain curve is used to analysis circuit stability. Here,  $Z_1$  and  $P_1$  represent the zero and pole frequencies of the noise gain curve, respectively.  $F_0$  is the uncompensated crossover frequency (noise gain curve intersecting open-loop gain).  $F_c$  represents the compensated crossover frequency (0 dB point) after stabilization. The expressions for  $Z_1$ ,  $P_1$ ,  $F_0$ ,  $F_c$  are given by Eqs. (8)–(11).

$$Z_1 = \frac{1}{2\pi R_f(C_s + C_f)} \quad (8)$$

$$P_1 = \frac{1}{2\pi R_f C_f} \quad (9)$$

$$F_0 = \sqrt{Z_1 \text{GBP}} \quad (10)$$

$$F_c = \frac{\text{GBP}}{1 + \frac{C_s}{C_f}} \quad (11)$$

The noise gain curve is determined by Eq. (12). If  $C_f$  is too small or  $R_f$  is sufficiently small, the noise gain curve will intersect with the open-loop gain curve at the red point. At this crossover frequency, the combined

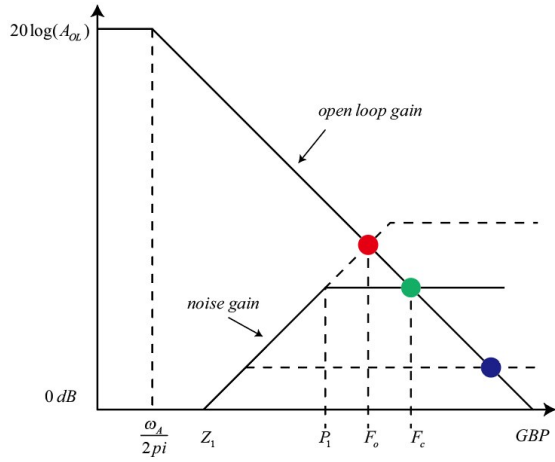


Fig. 4 Co-plot of the open-loop gain curve and noise gain curve.

图4 开环增益和噪声增益仿真曲线

slope of the open-loop and noise gain results in a -40 dB/decade roll-off in the closed-loop response. In this case, the phase margin is typically less than  $45^\circ$ , indicating that the circuit operates in an unstable state and is prone to oscillate. Adding  $C_f$  introduces a pole after the zero point in the noise gain response, as shown in Eq. (12).

$$G(\omega) = \frac{j\omega R_f(C_s + C_f) + 1}{j\omega R_f C_f + 1} \quad (12)$$

This compensation modifies the noise gain profile such that at the new crossover frequency (green point), the closed-loop gain exhibits a +20 dB/decade slope. The resulting phase margin improvement stabilizes the circuit operation. However, excessive  $C_f$  will shift the compensation pole to lower frequencies, causing the noise gain curve to intersect the open-loop gain at the blue point. In this case, the phase margin is also likely to be less than  $45^\circ$ , potentially causing conditional stability with peaking in the frequency response. As a rule of thumb,  $C_f$  should be smaller than  $C_s/G_{\min}$ , where  $C_s$  is the detector capacitance and  $G_{\min}$  is the minimum stable gain for a specific operational amplifier. In the context of OPA847, an operational amplifier with a GBP of 3.9 GHz, the value of  $G_{\min}$  is specified as 12.

Based on the preceding analysis, incorporating a properly sized feedback capacitance  $C_f$  is an effective compensation technique to ensure circuit stability.

### 3.3 Noise calculation

In lidar application, noise performance is crucial for information extraction. As shown in Fig. 5, a noise model of the read-out circuit is established. In the model, the primary sources of noise include the operational amplifier's input current noise, input voltage noise, thermal voltage noise, and low-frequency noise<sup>[24, 25]</sup>. Since low-frequency noise is usually below 1 kHz and contributes a small portion to the overall noise, it can be omitted to simplify the noise calculation.

As shown in Eq. (13), the power of noise can be summed up to calculate the equivalent input current  $i_{eq}$ ,  $i_n$  is the input current noise and  $e_n$  is the input voltage

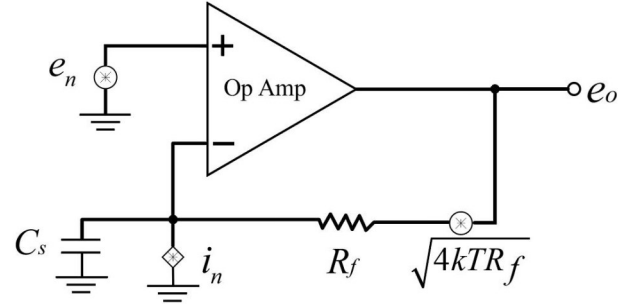


图5 读出电路的噪声模型: Fig. 5 Noise model of the read-out circuit.

noise of the operation amplifier. To determine the average power of the noise, the fourth term in Eq. (13) is integrated from zero to the bandwidth  $F$  as indicated in Eq. (14). Then the RMS value of the equivalent input current  $i_{eq}$  can be obtained using Eq. (15). This equation provides a easy noise evaluation method and can be used to optimize the noise performance by adjusting parameters such as  $R_f$ ,  $C_s$ , and  $F$ .

$$i_{eq}^2 = i_n^2 + \frac{4kT}{R_f} + \frac{e_n^2}{R_f^2} + e_n^2(2\pi f C_s)^2 \quad (13)$$

$$\frac{1}{F} \int_0^F (2\pi e_n f C_s)^2 df = \frac{(2\pi e_n C_s F)^2}{3} \quad (14)$$

$$\text{RMS}(i_{eq}) = \sqrt{i_n^2 + \frac{4kT}{R_f} + \left(\frac{e_n}{R_f}\right)^2 + \frac{(2\pi e_n C_s F)^2}{3}} \quad (15)$$

### 3.4 Detailed design of the balanced detector

Transimpedance circuits have been utilized in various applications<sup>[26-28]</sup>. In many cases, they are configured in a high-gain mode to sample the temporal waveform of the current signal, resulting in a relatively low bandwidth. For CDWL applications, the focus is on the signal spectrum, so bandwidth is a more important indicator than waveform<sup>[29, 30]</sup>.

PIN diodes which operate at the 2  $\mu\text{m}$  wavelength with low capacitance proved challenging. After extensive research, we selected G12182 PIN diodes for our balanced detector. These diodes have a relatively large capacitance of 30 pF per diode at a 0mV bias voltage, posing a challenge for meeting bandwidth requirements.

Considering the bandwidth requirements and noise performance, an operational amplifier with high GBP of 3.9 GHz, i. e., OPA847 from Texas Instruments, is chosen as the amplifier for this circuit. Moreover, the operational amplifier exhibits a low input current noise of 2.7 pA/ $\sqrt{\text{Hz}}$ , which is significant for transimpedance circuits, as the primary contribution of the operation amplifier to the noise is the input current noise rather than the input voltage noise. The detailed design of the balanced detector circuit is shown in Fig. 6. Two identical PIN diodes are connected in series to form a balanced detection circuit, which helps eliminate common-mode noise. Components  $R_1$ ,  $C_1$ ,  $R_2$ , and  $C_2$  are used to form RC low-pass filters, providing clean bias voltages. Addi-



tionally, a resistor  $R_3$  is placed at the negative input of the operational amplifier for offset cancellation. A capacitance  $C_3$  is placed in parallel with  $R_3$  to filter out the thermal noise generated by  $R_3$ .

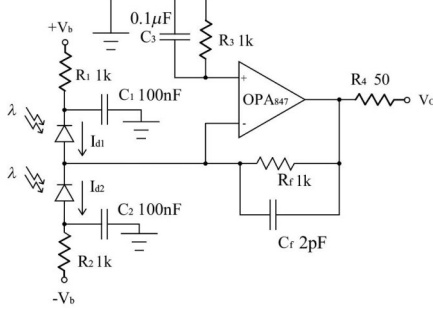


Fig. 6 Balanced detector circuit design.  
图6 平衡探测器电路设计

The circuit parameters were carefully chosen to achieve a maximally flat response. In common cases, the bias voltage is set to 0 mV to minimize the dark current, allowing the capacitance of a single PIN detector to remain at 30 pF. The differential capacitance of the operational amplifier, denoted by  $C_{diff}$ , is 2 pF, while the common-mode capacitance of the operational amplifier, denoted by  $C_{cm}$ , is 1.7 pF. Then the total capacitance  $C_s$  can be calculated as 63.7 pF using Eq. (16). By introducing a feedback capacitance  $C_f = 2$  pF, a bandwidth of 113 MHz with a maximally flat response according to Eq. (4)–(5) is achieved.

$$C_s = 2 \times C_{PIN} + C_{diff} + C_{cm} \quad (16)$$

For low-noise operation, attention should not only be given to the amplifier design but also to the power supply. We have employed low-noise LDOs, including MIC5205 and LT1964, to supply a low-noise power source of +5V and -5V, respectively. Moreover, 10uF, 0.1uF, and 0.01uF power supply filtering capacitors are placed near the amplifier's power pads to further improve the power quality, ensuring novel noise performance of the detector. Printed circuit board (PCB) design is also

important for circuit performance. As shown in Figure. 8, double-layer boards are used in the circuit design to minimize the parasitic capacitance. Minimizing the length of signal tracks in critical connections is critical to reduce track parasitic inductance and capacitance. However, the implementation of fiber adapters should also be considered. In addition, copper under the pads of the  $R_f$  and the feedback node of the amplifier were cut to decrease the parasitic capacitance.

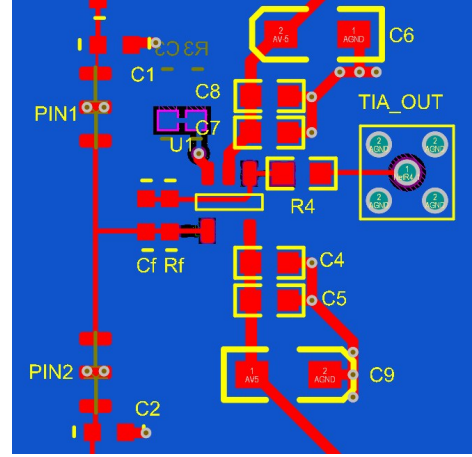


Fig. 7 The detector circuit layout.  
图7 探测器电路布局结构

## 4 Experiments and results

### 4.1 Experiments preparation

To verify the detector performance, a test module is set up, which incorporates the detector with a custom-built DAQ and is connected to a host PC for data transmission and processing.

As shown in Fig. 8, the DAQ serves as a dependent part of the test module. Its main function is to digitize the analog output signal, process the data, and transfer data to the PC. To meet the requirements for bandwidth and accuracy, a high sampling rate Analog-to-Digital Converter (ADC) is required. To perfectly reconstruct a bandlimited signal, the sampling rate must exceed twice the signal's highest frequency component, as mandated

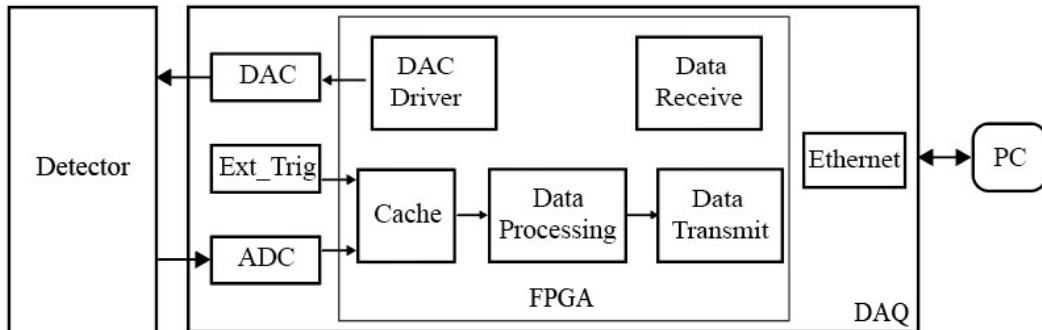


Fig. 8 Test module diagram.  
图8 测试模块结构框图

by the Nyquist-Shannon sampling theorem. Therefore, the sampling rate of the data acquisition module must exceed 220 mega-samples per second (Mps). For redundancy, a 500 Mps ADC was implemented. Meanwhile, a Field Programmable Gate Array (FPGA) is employed to interface with the ADC and enable real-time data transmission. A 1000 Mbps Ethernet is established for communication with the PC.

In addition, a two-channel DAC is utilized to provide bias voltages to the PIN diodes. The DAC output is controlled through a serial peripheral interface (SPI). Furthermore, an external trigger module is integrated to support external synchronous sampling via external triggering.

During measurement, the backscatter signal is transformed into current in the detector, which is then converted into analog signal through read-out circuit and digitized in the DAQ with the external-trigger signal. The waveform data are then transferred to a PC for postprocessing, such as Fast Fourier Transform (FFT) and power spectrum density analysis.



Fig. 9 The photo of the test module  
图9 测试单元实物图

As shown in Fig. 9, the detector and the DAQ are co-packaged in an aluminum box with dimensions of 55 mm  $\times$  110 mm  $\times$  150 mm. Two angled physical contact (APC) couplers are placed in the front panel for laser coupling. In the back panel, an RJ-45 interface, an ex-

ternal trigger interface, and a power input interface are provided.

#### 4.2 ADC frequency response test

Before evaluating the detector's bandwidth and frequency response, the ADC's frequency response must be determined. An arbitrary function generator (AFG) is employed to provide sine signals sweeping from 10 MHz to 250 MHz in 10 MHz steps. The frequency response is measured at each frequency point, with 1,000 acquisitions averaged to ensure statistical significance. As depicted in Fig. 10, the -3 dB bandwidth of the ADC is close to 178 MHz, enabling following detector frequency response calibration and test.

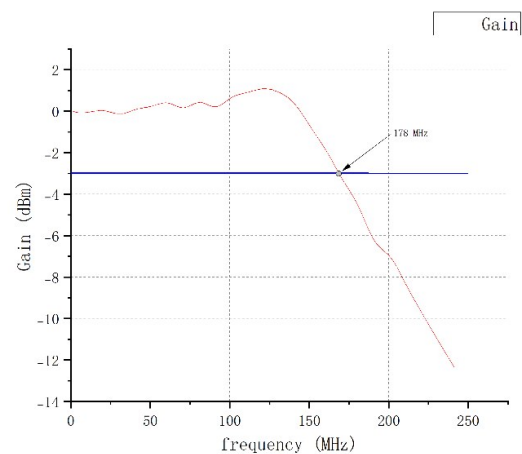


Fig. 10 ADC frequency response test.  
图10 ADC 频率响应测试

#### 4.3 Background noise test

An experimental platform was constructed as shown in Fig. 11, a commercial AFG is utilized to offer sine wave with fixed offset to drive the laser source, the laser output is coupled to one of the detector's inputs through an optical fiber, detected and digitized in the device under test (DUT). Then the signal scope is transmitted to a PC via data transmission interface.

To test and verify the noise performance of the detector, the detector is placed inside a dark box to ensure that no background light is coupled into the detector.

Given the unavailability of commercial detectors operating at the same wavelength of 2  $\mu\text{m}$ , we employed

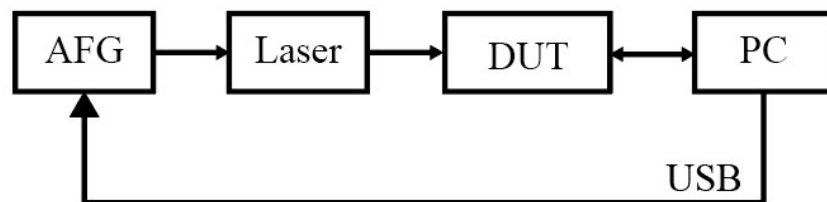


Fig. 11 Test platform diagram.  
图11 测试平台原理框图

the Thorlabs PDB465c detector for detector noise comparison.

As shown in Fig. 12, the noise histograms are generated and fitted with Gaussian functions, respectively. The standard deviation of Gaussian function, namely the RMS noise value, is determined to be  $539\ \mu\text{V}$  for our detector, and the offset voltage is found to be  $-620\ \mu\text{V}$ . Meanwhile, the background noise of the commercial detector has an RMS noise value of  $2.28\ \text{mV}$ , with a offset voltage of  $-3.81\ \text{mV}$ . In comparison, our detector exhibits lower background noise and better offset cancellation performance.

#### 4.4 Detector frequency response test

To determine the frequency response of each diode in the detector, a sine wave from  $1\ \text{MHz}$  to  $150\ \text{MHz}$  in  $1\ \text{MHz}$  steps is generated by AFG to drive the laser. Then peak-to-peak voltage of the sampling waveform is recorded at each point. The ADC frequency response and the laser frequency response from product datasheet are used for calibration. The normalized results are presented in Fig. 13. From the plot, it can be observed that the  $-3\ \text{dB}$  bandwidth is measured to be  $110.8\ \text{MHz}$  and  $110.3\ \text{MHz}$ , respectively, which satisfies the requirements of bandwidth. In addition, the response is flat enough, which facilitates the peak finding. The results show that the detector detects the laser signal within the required bandwidth, while the frequency responses of the two diodes are consistent with each other.

#### 4.5 Bias voltage impacts investigation

Bandwidth is a critical metric in lidar application. Increasing the bias voltage reduces PIN diodes capacitance  $C_s$ , thereby extending the bandwidth. However, this bandwidth enhancement is achieved at the expense of increased dark current, which degrades the noise performance through enhanced shot noise. For diodes with relatively large capacitance, bias voltage needs to be employed for higher bandwidth. In order to evaluate the impact of bias voltage on noise and bandwidth, the bias voltage is swept from  $0\ \text{mV}$  to  $1000\ \text{mV}$  within the diodes's specified operating range. In specific, the bias voltage is adjusted at intervals of  $100\ \text{mV}$ . At each bias voltage, the bandwidth and noise values of the circuit are measured.

As shown in Fig. 14, the bandwidth increases from  $110\ \text{MHz}$  to  $159\ \text{MHz}$ , which represents a  $1.45\times$  increase in bandwidth through bias voltage tuning. And it is noted that the bandwidth increase rate becomes slower with rising bias voltage. The relationship between noise and bandwidth are shown in Fig. 15. The RMS value of the output noise increases linearly from  $0.54\ \text{mV}$  to  $0.6\ \text{mV}$ , representing a  $1.1\times$  increase in noise, due to both the dark current and the increased bandwidth, which are consistent with the Eq. (15). Thanks to data extraction method employed in the CDWL system, the noise degradation can be compensated by a  $1.1\times$  increase in signal averaging time, enabling a large wind speed detection range. From the results, it can be concluded that adjusting the bias voltage can increase the bandwidth while not significantly degrade the noise performance. Therefore, employing the bias voltage is an efficient approach to enhance the circuit's bandwidth if higher wind speed detection range is required.

## 5 Conclusion

The  $2\ \mu\text{m}$  wavelength laser enables extended detection ranges due to superior atmospheric transmission in the infrared window and higher laser power, necessitating comprehensive investigation of  $2\ \mu\text{m}$  detectors. In our work, a balanced detector operates at  $2\ \mu\text{m}$  has been developed to enable preliminary research for  $2\ \mu\text{m}$  CDWL systems. To meet the bandwidth requirements, a transimpedance circuit with highspeed operational amplifier has been implemented. Moreover, a DAQ was incorporated with the detector for data transmission and control, based on which the detector performance is evaluated. In addition, the impact of bias voltage tuning on bandwidth and noise has been investigated. Results show that the detector meet the bandwidth requirements and can support higher bandwidth requirements via bias voltage tuning. These findings can serve as a valuable reference for researchers and professionals in the field.

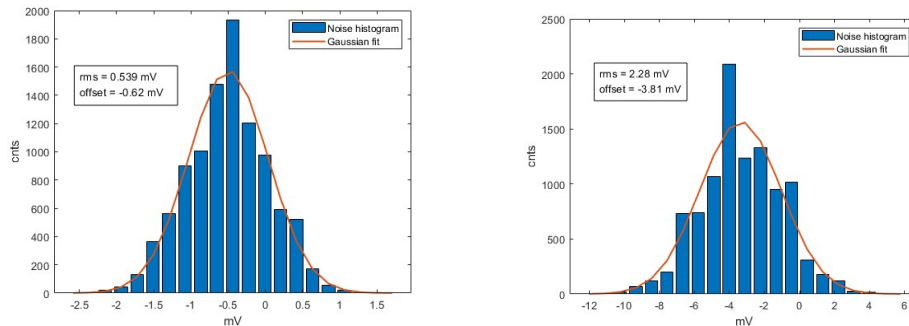


Fig. 12 (a)The noise histogram of our detector(b)The noise histogram of the commercial detector  
图 12 (a)自研探测器噪声直方图(b)商用探测器噪声直方图



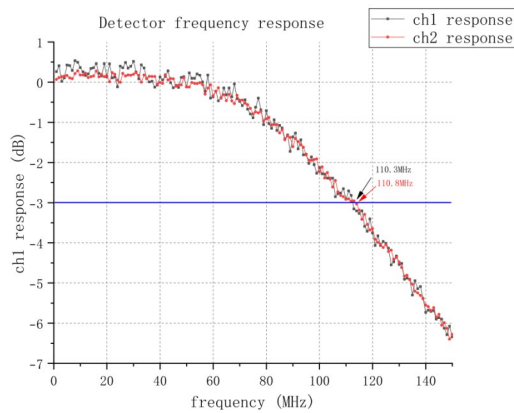


Fig. 13 Detector frequency response.  
图 13 探测器频率响应

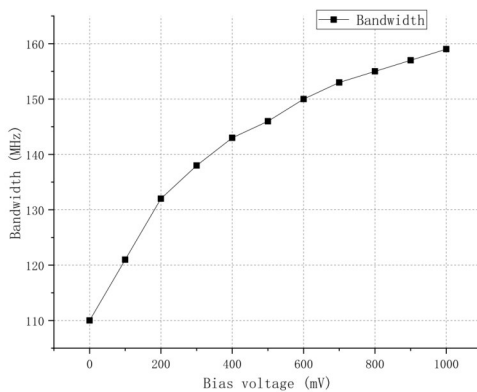


Fig. 14 Detector bandwidth vs bias voltage.  
图 14 探测器带宽与偏置电压的关系

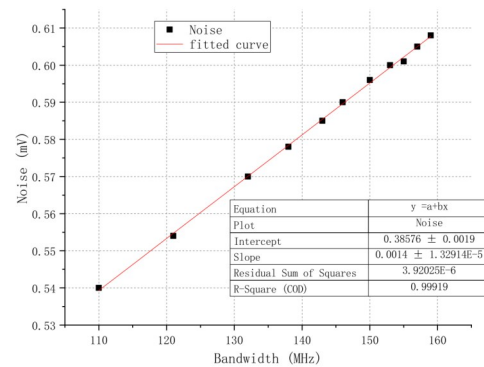


Fig. 15 Detector noise vs bandwidth.  
图 15 探测器噪声与带宽的关系

## Acknowledgment

We gratefully acknowledge the Optical Quantum Lidar Research Group (USTC) for their platform support during the experimental process. We also acknowledge the Hefei National Laboratory for their valuable suggestions. The project was supported by the National Key R&D Program of China under Project No. 2022YFB390

3103.

## References

- [1] WEI T, WANG M, JIANG P, et al. Retrieving aerosol backscatter coefficient using coherent Doppler wind lidar [J]. *Optics Express*, 2025, 33(4): 6832--49.
- [2] SU L, XIA H, YUAN J, et al. Study on Daytime Atmospheric Mixing Layer Height Based on 2-Year Coherent Doppler Wind Lidar Observations at the Southern Edge of the Taklimakan Desert [J]. *Remote Sensing*, 2024, 16(16): 3005.
- [3] YUAN J, WU K, WEI T, et al. Cloud seeding evidenced by coherent Doppler wind Lidar [J]. *Remote Sensing*, 2021, 13(19): 3815.
- [4] XIA H, CHEN Y, YUAN J, et al. Windshear Detection in Rain Using a 30 km Radius Coherent Doppler Wind Lidar at Mega Airport in Plateau [J]. *Remote Sensing*, 2024, 16(5): 924.
- [5] FUJII T, FUKUCHI T. Elastic Lidar Measurement of the Troposphere [M]. *Laser Remote Sensing*. 2005: 81--140.
- [6] LOLLI S, DELAVAL A, LOTH C, et al. 0.355- $\mu\text{m}$  direct detection wind lidar under testing during a field campaign in consideration of ESA's ADM-Aeolus mission [J]. *Atmospheric Measurement Techniques*, 2013, 6(12): 3349--58.
- [7] LUX O, REICHERT R, LEMMERZ C, et al. CCD detector performance of the space-borne Doppler wind lidar ALADIN during the Aeolus mission [J]. *Applied Optics*, 2024, 63(25): 6754--75.
- [8] LIU Z, YUAN L, TANG J, et al. Coherent Doppler lidar wind retrieval for a typhoon based on the genetic simulated annealing algorithm [J]. *Chinese Optics Letters*, 2024, 22(4): 040101.
- [9] LIU Z, ZHANG Y-P, ZHU X-P, et al. Decoupling of temporal/spatial broadening effects in Doppler wind LiDAR by 2D spectral analysis [J]. *Chinese Physics B*, 2024, 33(3): 034214.
- [10] CAADILLAS B, BECKENBAUER M, TRUJILLO J J, et al. Off-shore wind farm cluster wakes as observed by long-range-scanning wind lidar measurements and mesoscale modeling [J]. *Wind Energy Science*, 2022, 7(3): 1241--62.
- [11] KARLSSON C J, OLSSON F A, LETALICK D, et al. All-fiber multifunction continuous-wave coherent laser radar at 1.55  $\mu\text{m}$  for range, speed, vibration, and wind measurements [J]. *Applied optics*, 2000, 39(21): 3716--26.
- [12] TANG L, SHU Z, DONG J, et al. Mobile Rayleigh Doppler wind lidar based on double-edge technique [J]. *Chinese Optics Letters*, 2010, 8(8): 726--31.
- [13] LONG W, DAI G, WU S, et al. Simulation and assessment of space-borne hybrid Doppler wind lidar, Part 1: the spaceborne two-beam stepping direct detection Doppler wind lidar [J]. 2024.
- [14] ZHANG J, CHEN Z, LU Y, et al. Characteristics of aerosol size distribution and vertical backscattering coefficient profile during 2014 APEC in Beijing [J]. *Atmospheric Environment*, 2017, 148: 30--41.
- [15] TRUJILLO J J, RETTENMEIER A, SCHLIPF D. Arrangements for enhanced measurements of a large turbine near-wake using LiDAR from the nacelle [Z]. 2008: 012060.
- [16] DONG D, YANG S, WENG N, et al. Analysis of Observation Performance of a Mobile Coherent Doppler Wind Lidar Using DBS Scanning Mode [Z]. 2021: 012048.
- [17] DAI Y, LIANG H, WU Q, et al. Structure optimization of high speed space coherent optical balance detectors [J]. *Optics and Precision Engineering*, 2017, 25(10): 2736--43.
- [18] NAG D, YAO W, VAN DER TOL J J G M. Optimization of balanced detector for coherent receiver on generic InP platform by particle swarm optimization [J]. *IEEE Journal of Quantum Electronics*, 2024, 60(3): 1--12.
- [19] LU Q, SHEN Q, CAO Y, et al. Ultra-low-noise balanced detectors for optical time-domain measurements [J]. *IEEE Transactions on Nuclear Science*, 2018, 66(7): 1048--55.
- [20] YANG H, WANG C, XUE X, et al. High-accuracy vertical wind profiling up to 12 km using a 1064 nm coherent Doppler Lidar with 10 mJ pulsed laser [J]. *Optics Express*, 2025, 33(7): 15241--53.
- [21] WANG C, YANG K, QU L, et al. Coherent two-photon atmospheric lidar based on up-conversion quantum erasure [J]. *ACS Photonics*, 2024, 11(9): 3528--35.
- [22] QIANG W, WANG C, WANG Y, et al. All-fiber multifunction differential absorption CO<sub>2</sub> lidar integrating single-photon and coherent detection [J]. *Optics Express*, 2024, 32(11): 19665--75.
- [23] ALBRECHT H E, DAMASCHKE N, BORYS M, et al. Laser Dop-

- pler and phase Doppler measurement techniques [M]. 2013.
- [24] JOHNSON J B. Thermal agitation of electricity in conductors [J]. Physical review, 1928, 32(1): 97.
- [25] WANG S, XIANG X, ZHOU C, et al. Simulation of high SNR photo-detector with LC coupling and transimpedance amplifier circuit and its verification [J]. Review of Scientific Instruments, 2017, 88(1): 013107.
- [26] MASETTI E, CATTINI S, ROVATI L. A transimpedance preamplifier using a feedforward approach for robust rejection of DC photogenerated currents [J]. Review of Scientific Instruments, 2023, 94(1).
- [27] VELSINK M C, ILLIENKO M, SUDERA P, et al. Optimizing pump--probe reflectivity measurements of ultrafast photoacoustics with modulated asynchronous optical sampling [J]. Review of Scientific Instruments, 2023, 94(10).
- [28] FANG S, YIN B, XIE W, et al. Low-noise and high-speed transimpedance amplifier for nanopore sensor [J]. Review of Scientific Instruments, 2023, 94(7).
- [29] GARCIA E, BALES C, PATTERSON W, et al. Cryogenic probe for low-noise, high-frequency electronic measurements [J]. Review of Scientific Instruments, 2022, 93(10).
- [30] MUTHUKUMARAN B, RAMACHANDRAN B. High Gain CMOS Transimpedance Amplifier For Near Infrared Spectroscopy Applications [Z]. 2022: 012039